Title

Structural Evaluation of Steel–Concrete Joint with UHPC Grout in Single Cable–Plane Hybrid Cable-Stayed Bridges

Journal

Journal of Bridge Engineering, 24(4)

ISSN

1084-0702

Authors

He, Shaohua
Mosallam, Ayman S
Fang, Zhi
et al.

Publication Date

2019-04-01

DOI

10.1061/(asce)be.1943-5592.0001379

Peer reviewed

Structural Evaluation of Steel–Concrete Joint with UHPC Grout in Single Cable–Plane Hybrid Cable-Stayed Bridges

Shaohua He[1]; Ayman S. Mosallam, F.ASCE[2]; Zhi Fang, Ph.D.[3]; and Liyang Liu[4]

Abstract: In order to investigate the mechanical behavior of the steel–concrete joint with ultrahigh performance concrete (UHPC) grout in single cable–plane hybrid cable-stayed bridges, a model test with a scale of 1:3 for a hybrid girder consisting of a flat steel box girder, a prestressed concrete (PC) box girder, and a steel–concrete joint connecting the steel and prestressed concrete girders was conducted. Structural responses of large-scale specimens under combined actions of axial compression, bending, and twisting moments are presented and discussed. Experimental results indicated that steel–concrete joints with UHPC grout exhibited favorable combined behavior and adequate strength. Under a maximum applied load that is twice as much the design load, the system components, including surface plates/slabs, UHPC, perforated webs, and perforated rebars, behaved within the elastic range. Stresses generated at the steel–concrete joint were mainly determined by axial and flexure forces. The influence of torsion on joint behavior was insignificant. It was also shown that approximately 65% of the overall force transferred through the steel–concrete joint was in the form of compression effects between the bearing steel plate and UHPC, and that the remaining 35% force was dispersed via shear connectors. Furthermore, finite-element (FE) models were developed and calibrated with the experimental results. The numerical results indicated that load transferred via the bearing plate compression effect gradually increased with the steel cell height. The outcomes of this study provide a reference for future application of the steel–concrete joint with UHPC in hybrid girder bridges. **DOI: 10.1061/(ASCE)BE.1943-5592.0001379.**

Author keywords: Hybrid cable-stayed bridge; Steel–concrete joint; UHPC grout; Model test; Mechanical behavior; Numerical simulation.

Introduction

The steel–concrete hybrid girder, incorporating steel and reinforced concrete girders into a single integrated girder, has been considered as an important advancement in the application of steel/concrete composite structures. The concept of hybrid cable-stayed bridges, using steel girders at the middle-spans and prestressed concrete (PC) girders at the side-spans was proposed first in the 1970s. The application of hybrid girders in cable-stayed bridges offers many advantages. For example, steel girders at the middle-spans can effectively resist tensile stresses and increase the maximum span length of the bridge. The utilization of PC girders at the side-spans can help in balancing the self-weight of the long middle-span, increasing bridge girders stiffness. Since the construction of the Kurt-Schumacher Bridge in Germany (Volke 1973), that is considered to be the first hybrid cable-stayed bridge, numerous hybrid cable-stayed bridges have been built around the world, such as the Normandie Bridge in France (Virlogeux 1994), the Tatara Bridge in Japan (Endo et al. 1991), the Bunker Hill Bridge in the United States (Chandra et al. 2003), and many others.

Steel–concrete joints connecting steel and concrete girders is the key component for assuring an optimal performance of such hybrid girder bridges. Several types of steel–concrete joints have been developed. One of the popular steel–concrete joints is in the form of concrete-filled steel cells (CFSCs) and shear connectors (Nie 2011). According to the presence of bearing plates, the joint with CFSCs can be categorized as: (1) steel cells with front bearing plates [Fig. 1(a)]; (2) steel cells with rear bearing plates [Fig. 1(b)]; and (3) steel cells with both front and rear bearing plates [Fig. 1(c)]. These types of joint details have the benefits of the steel cells that serve as a convenient framework for casting concrete, providing confinement for the core concrete, and preventing the concrete from spalling when overloaded. To date, the steel–concrete joint with CFSCs has been gradually used in many hybrid girder bridges (Gimsing 1997; Ohlsson 1996; Zhang et al. 2014).

Mechanical behavior of steel–concrete joints with CFSCs in hybrid cable-stayed bridges has been evaluated by several researchers. He et al. (2014) examined the safety and reliability of steel–concrete joints in the Jingyue Bridge. The experimental results showed that approximately 55 and 45% of the axial loads in the joint zone were carried by the bearing plate and shear connectors, respectively. Zhang and Wu (2013) and He et al. (2012) investigated the load transfer path of the steel–concrete joint of the Jiujiang Bridge. The results indicated that nearly 70 and 30% of the overall loads were dispersed by bearing plate and shear connectors, respectively. Yao et al. (2014) and Ye et al. (2015) studied the behavior of a steel–concrete joint in the Yongjiang Bridge. The results indicated that the joint bearing capacity sharply decreased with the occurrence of separation at the steel–concrete interface. Zhang et al. (2010a) performed a 1:2 scale model test and several numerical simulations on the Yingxiong Bridge steel–concrete joint. The results showed that the joint offered the favorable bearing

[1]Assistant Professor, School of Civil and Transportation Engineering, Guangdong Univ. of Technology, Guangzhou, Guangdong 510006, China.

[2]Professor, Dept. of Civil and Environmental Engineering, Univ. of California, Irvine, CA 92697.

[3]Professor, College of Civil Engineering, Hunan Univ., Changsha, Hunan 410082, China (corresponding author). Email: fangzhi@hnu.edu.cn

[4]Engineer, Broadvision Engineering Consultants, Kunming, Yunnan 650011, China.

Note. This manuscript was submitted on May 15, 2018; approved on October 10, 2018; published online on February 14, 2019. Discussion period open until July 14, 2019; separate discussions must be submitted for individual papers. This paper is part of the ***Journal of Bridge Engineering***, © ASCE, ISSN 1084-0702.

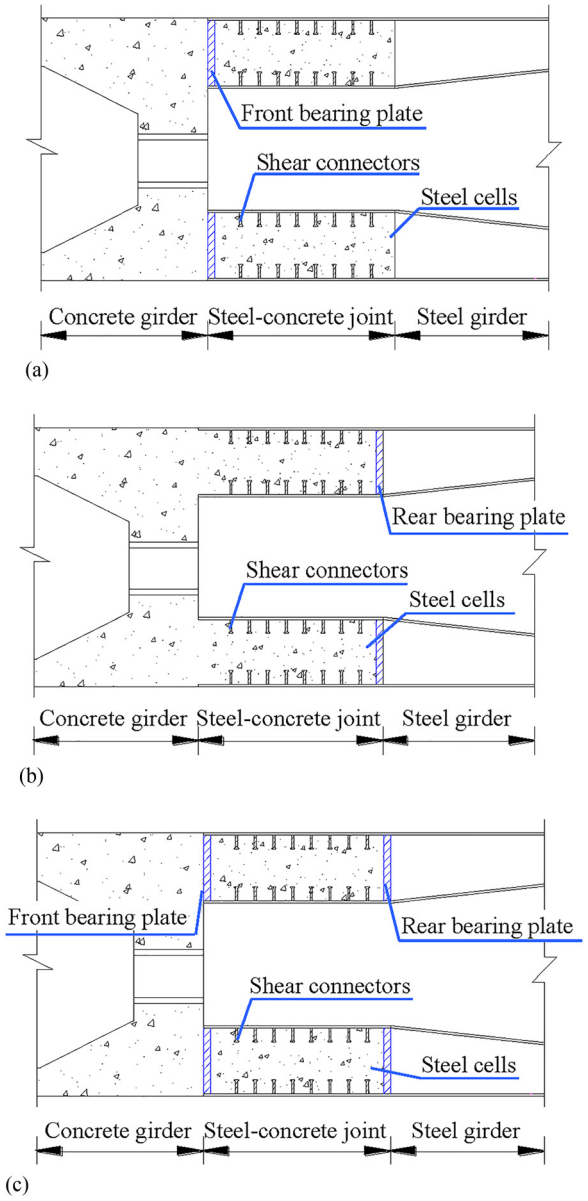

Fig. 1. Steel–concrete joint with CFSCs: (a) steel cells with front bearing plate; (b) steel cells with rear bearing plate; and (c) steel cells with both front and rear bearing plates.

capacity to the hybrid girder. Liu et al. (2010) evaluated load transfer mechanism of the Edong Bridge steel–concrete joint. They reported that approximately one-half of the axial force was transferred by both the bearing plate and the shear connectors, respectively.

The majority of the aforementioned published studies focused mainly on the performance of the steel–concrete joints in hybrid cable-stayed bridges with double cable-planes, where the joint is mainly subjected to axial, flexure, and shear forces. However, for a single-plane hybrid cable-stayed bridge with the cables distributed along or near the girder's longitudinal center axis, the steel–concrete joint should not only carry the loads referred above but also resist the torque introduced by traffic loads. The load and boundary conditions of the steel–concrete joint in single-plane hybrid cable-stayed bridges are significantly different from those of bridges with double cable-planes. Thus, it is necessary to investigate the mechanical behavior of steel–concrete joint in single-plane hybrid cable-stayed bridges and evaluate the impact of the torque on joint performance.

Despite the fact that steel–concrete joints with CFSCs have been utilized in existing hybrid cable-stayed bridges, in some cases, many obstacles were identified including: (1) the need of numerous shear connectors to resist the axial forces, resulting in complex geometric dispositions and installation difficulties; (2) the potential interweave of steel reinforcements and prestressing tendons in small steel cells, leading to difficulties in achieving the desired quality of concrete grout; (3) the separation between steel and concrete resulted from concrete shrinkage, decreasing the safety and durability of such joints (Ye et al. 2015); and (4) the existence of high-stress concentrations at the steel cells that affect the strength of conventional concrete (Ji et al. 2009; Liu and Liu 2015). The use of ultrahigh performance concrete (UHPC) as steel–concrete joint grout could provide a solution to solve these problems. Previous studies indicated that the utilization of UHPC can improve the ultimate strength of shear connectors (Leonhard et al. 1987; He et al. 2017), thus fewer connectors may be required when UHPC is used. Also, the less creep and shrinkage of UHPC may result in a better bond and friction between the joint's steel components and concrete. Another benefit of using UHPC is the ease of placing concrete at the joint zone due to the absence of coarse aggregates. However, to date, research on the steel–concrete joint with UHPC grout has not been reported.

Fig. 2 presents the recently constructed single-plane hybrid cable-stayed Nujiang Bridge with a span arrangement of 81.0 + 175.0 m, located in Yunan, China. The steel–concrete joint in the hybrid girder of this bridge consists of several CFSCs with the rear bearing plate and shear connectors. Based on the geometric configurations of the Nujiang Bridge, this paper explores the load transfer mechanisms in steel–concrete joints with UHPC grout. The feasibility of the use of UHPC as a core grout for the steel–concrete joint is evaluated by testing a 1:3 scale-down model of the joint in the researched bridge. Stress and displacements generated at different locations of the test specimen under combined loads of axial compression, flexure, and twisting moments were recorded and analyzed. Furthermore, numerical simulation models were established and calibrated via experimental results, and the influence of varying the steel cell height on the joint behavior was evaluated by conducting a parametric study.

Design of Large-Scale Test Model

Test Model Description

The large-scale test model replicated the steel–concrete joint of the Nujiang Bridge [Fig. 2(c)]. Considering the limitations of testing facilities and the law of similarity, the test specimen was designed with a scale-down of 1:3. Fig. 3 gives the details of the bridge test model evaluated experimentally in this study. As presented in Fig. 3(a), two rigid transoms were fabricated and placed at the ends of the specimen for the convenience of load application. The box cross sections with five cells for the PC and steel girders are given in Figs. 3(c and d), respectively. All geometric, physical, and boundary conditions satisfied the similarity theory. The height, width, and length of the model were reduced to one-third of the selected part from the present bridge. The flange area of box cross sections was relatively small as compared to the total sectional area; thus, the flanges were neglected for the test model.

Fig. 3(a) provides the 616.7 cm specimen consisted of a solid concrete transom, a PC girder, a steel–concrete joint, a steel girder, and a steel transom. The thicknesses of the top slab, bottom slab, and web of the PC girder were 12.0, 10.0, and 10.0 cm, respectively. The ratio of reinforcements in PC girder for the test specimen was

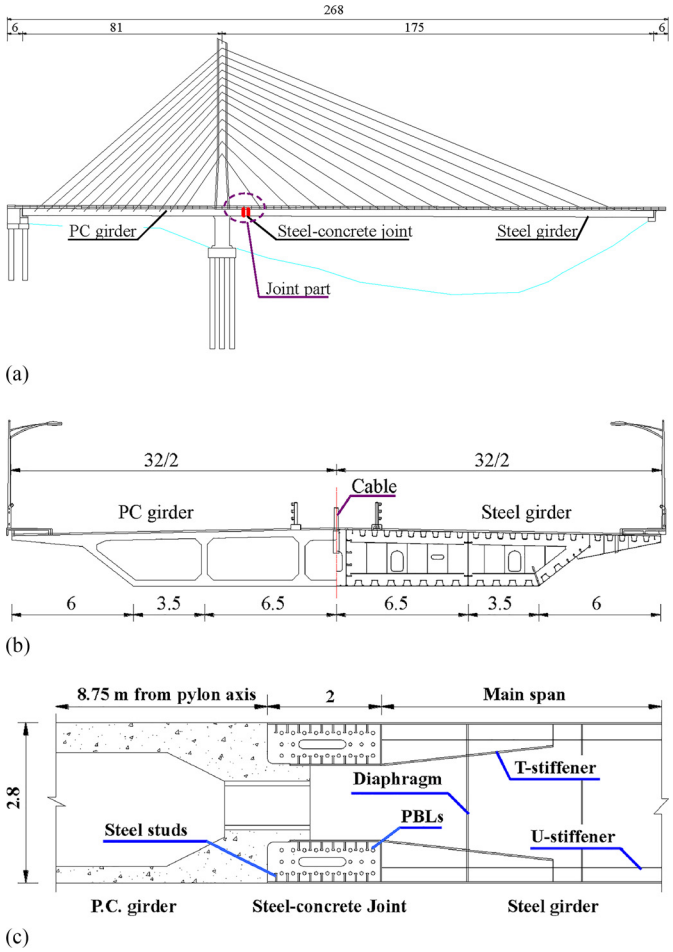

Fig. 2. Nujiang Bridge: (a) elevation view; (b) cross section of main girder; and (c) steel–concrete joint arrangement. (unit: m).

equivalent to that for the researched bridge. The prestressed strands with a diameter of 15.2 mm were fabricated consistent with their actual place in the bridge. The spherical bearing at the bottom of the concrete transom enabled the specimen to freely rotate about the axis of the specimen [Fig. 3(b)]. For the steel girder, orthotropic steel plates with a thickness of 8.0 mm located at the top and bottom were strengthened with 3.0 mm-thick U-shaped stiffeners. The use of T-shaped stiffeners with a thickness of 8.0 mm and a length of 988.0 mm adjacent to the steel–concrete joint are to strengthen both the top and bottom slabs. Steel plates with 11.0 mm thickness were used as the webs of the steel girder. As presented in Fig. 3(e), the steel transom was strengthened by a number of stiffeners. The spherical bearing at the transom bottom was to provide the free rotating ability for the specimen.

Details and Dimensions of the Steel–Concrete Joint

As stated previously, the dimensions for the members in the steel–concrete joint of the test specimen were scaled down to one-third of those for the Nujiang Bridge. As presented in Fig. 4(a), the total height of the cross section, the width of the top and bottom decks were 93.3, 833.4, and 666.7 cm, respectively. Fig. 4(b) shows the arrangements for a typical CFSC in the steel–concrete joint. The height of the steel cell was 250.0 mm, and the thickness of the top plate, bottom plate, rear bearing plate, and perforated webs was 8.0 mm. Steel studs with dimensions of 8.0 × 50.0 mm welded at the inner surfaces of the cells were used to prevent the possible separation between the steel and UHPC. Together with UHPC grout, the 8.0 mm-diameter steel rebars passing through the 20.0 mm-diameter holes in the perforated webs formed the perfobond strip (PBL) connectors, as illustrated in Fig. 4(c).

Experimental Program

Material Properties

The materials properties of the test specimen were the same as those of the researched bridge. The concrete compressive strength and modulus of elasticity of the PC girder and the concrete transom are 62.0 MPa and 36.1 GPa, respectively. The UHPC grout used to fill the joint is a commercially produced reactive powder concrete (RPC). The RPC is composed of ordinary Portland cement, silica fume, quartz sand, ground quartz, water reducer, concrete expansion agent, and short steel fibers. Table 1 provides the mix proportions of the RPC used in this study. The steel fibers were selected based on the experimental findings reported by Qin and Cao (1999), which revealed that the fibers with a length of 12–16 mm, a diameter of 0.15–0.22 mm, and a volume content of 1.5–3.0% contributed to the favorable properties of the RPC material. In the current tests, the steel fibers used for RPC had an average length of 15.0 mm, a diameter of 0.2 mm, a tensile strength of 2,600.0 MPa, and a volume content of 2.0%. As hot steam curing is not applicable for the joint in the construction site, the RPC was cast using the concrete mixture producing 100.0 MPa target compressive strength. Six standard cubes with a side length of 100.0 mm and twelve 100.0 × 100.0 × 300.0-mm prisms were used for determining the RPC properties (Hunan Province Dept. of Housing and Urban-Rural 2017). The cube specimens were used to measure the compressive strength, while the prism specimens were used to measure the prismatic strength and modulus of elasticity. Table 2 presents the average strength values obtained from testing specimens after curing for 28 days, where f_{cu} = cubic compressive strength; f_{cp} = prismatic strength; and E_c = modulus of elasticity.

Structural Q345C steel with a nominal yield strength of 345.0 MPa was used for all steel plates. HRB335 steel rebars, with a nominal yield strength of 335.0 MPa, were used for all internal reinforcements. The mechanical properties of the steel plates and reinforcements obtained from standard coupon tests are presented in Table 3, where f_y = yield strength; f_u = ultimate strength; and E_s = modulus of elasticity. The average ultimate strength of the prestressed strands tested according to the Chinese code (China Committee for Standardization 2014) was 1,878.0 MPa.

Fabrication of Test Specimen

The steel members of the test specimen were fabricated in a factory. The concrete transom, PC girder, and UHPC grout were cast after the steel members were delivered to the site. The fabrication of the specimen included three steps (Fig. 5): (1) assembly of the steel components into a single steel segment at the factory; (2) filling UHPC grout into steel cells and curing for three days [Fig. 5(b)]; finally, (3) completing the construction of the PC girder and the concrete transom. Fig. 5(c) shows the completed test specimen prior to testing.

Loading Procedure and Test Setup

Loading Scheme

The applied load protocol used in all tests was designed such that it generates specimen stresses equal to those are expected to be

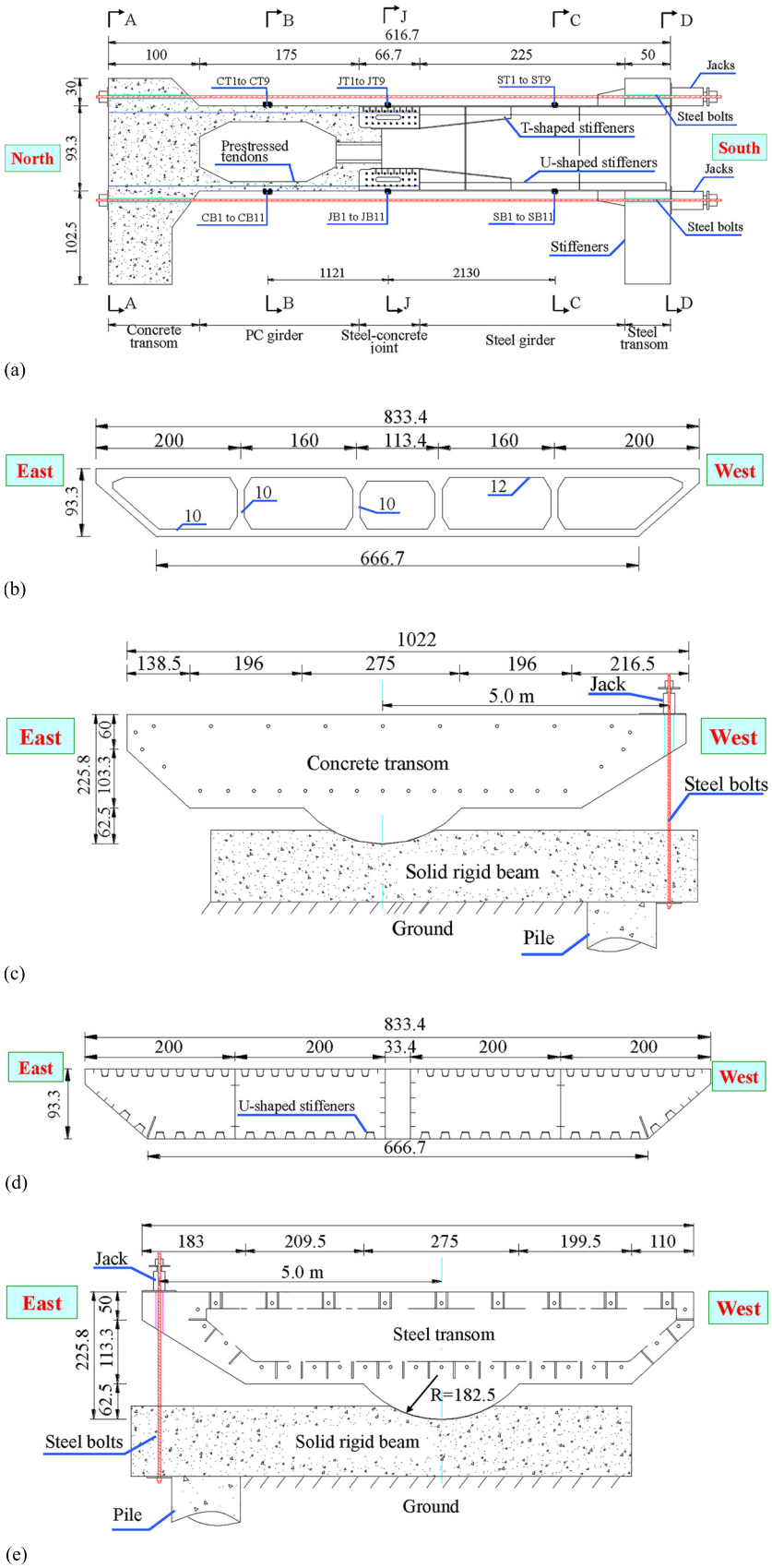

Fig. 3. Outline of test model: (a) elevation view; (b) concrete transom section (A-A); (c) PC girder section (B-B); (d) steel girder section (C-C); and (e) steel transom section (D-D). (unit: cm).

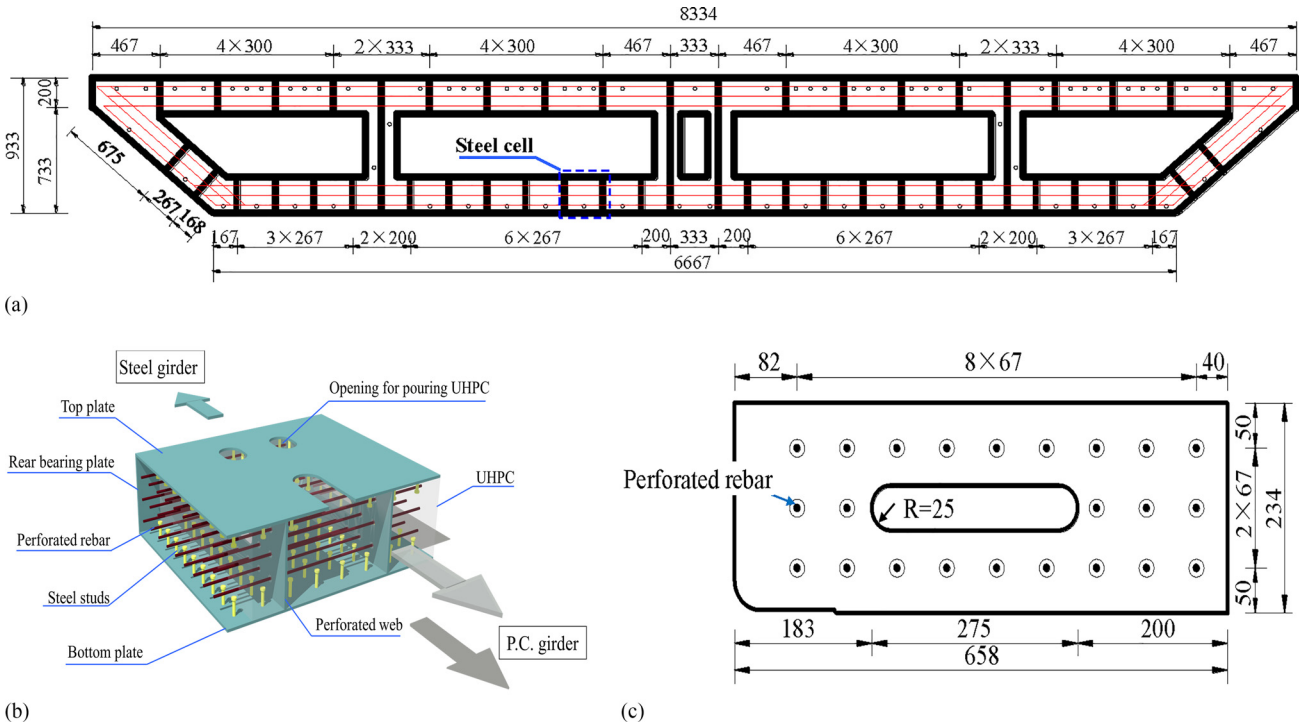

Fig. 4. Steel–concrete joint: (a) joint cross section (J-J); (b) arrangements of a typical steel cell; and (c) detailed dimensions for a perforated web. (unit: mm).

Table 1. RPC mix design

Material	Content
Cement	850.0
Silica fume	210.0
Quartz sand	930.0
Ground quartz	93.0
Water reducer	22.0
Expansion agent	70.0
Water	210.0
Steel fiber	2% vol.

Note: Unit in kg/m^3, except steel fibers in volume fraction.

Table 2. Mechanical properties of RPC material

Property	Value
Average f_{cu} (MPa)	116.0
Average f_{cp} (MPa)	84.0
Average E_c (GPa)	42.6

generated in the actual bridge. With considering both the dead and live loads, a load combination resulting in generating maximum axial force at the ultimate limit state was selected as the critical load combination, since the steel–concrete joint of the research bridge is mainly subjected to axial force. The design loads of the steel–concrete joint for the actual bridge and the test specimen are summarized in Table 4. Due to the lack of practical design methods in existing codes, the steel–concrete joint of the background bridge was designed based on the structural forms of early constructed joints, which were designed using the concept of safety factor. As such, Table 4 also includes the values of two

Table 3. Mechanical properties of steel reinforcements and plates

Item	Steel grade	Average f_y (MPa)	Average f_u (MPa)	Average E_s (GPa)
Steel reinforcements	HRB335	342.0	516.0	204.0
Steel plates	Q345C	374.0	525.0	210.0

times the design load since a minimum safety factor of 2.0 was required for the researched joint. It is noted that the shear force is comparatively small, and numerical simulation results indicated that the stresses generated from the shear forces are also negligible as compared to those induced by other forces. Therefore, only the axial force, flexure, and twisting moments were applied in the test. The negative axial force indicates that the joint is subjected to compression.

As presented in Table 4, "*N*," "*M*," and "*T*" denote the design load of axial force, bending moment, and torque, respectively. For the convenience of description, designation "*NMT*" and "*NM*" refer to load values of one-time design axial, bending, and torque loads and one-time design axial and bending loads, respectively. In order to examine the reliability of test equipment, the specimen was preloaded to 20% of the design axial, bending, and torque loads prior to the formal test. The applied loads used a force-controlled loading regime. The formal test procedure consisted of two load protocols: first, a load of 1.0NMT (one times the design axial, bending, and torque loads) was applied to examine the behavior of the specimen under design loads. The load was monotonically increased to 1.0NMT at a constant loading rate in five steps. In each loading step, the axial force was applied together with the bending moment, and in order to determine the influence of torque, the torque was applied five minutes after the application of the axial and bending loads in each step. In the

(a)

(b)

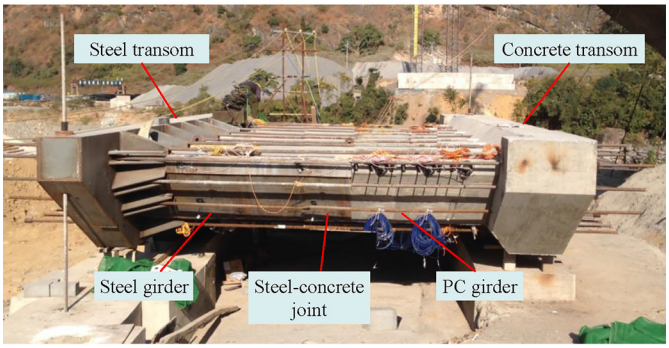

(c)

Fig. 5. Fabrication process for test specimen: (a) fabrication of steel segment in factory; (b) pouring UHPC into steel cells of steel–concrete joint; and (c) completion of test specimen.

second loading protocol, a load of 2.0NMT was applied in order to examine the joint margin of safety. The load was monotonically increased to 1.5NMT at a constant loading rate in three steps, and then gradually increased to 1.7 and 2.0NMT in two steps. The specimen was finally unloaded to zero at a constant unloading rate in five steps.

Table 4. Applied forces for research bridge and test specimen

Force	Research bridge		Test specimen	
	Design load (×1)	Design load (×2)	Design load (×1)	Design load (×2)
Axial force (kN)	−85,775	−171,510	−10,000 (*N*)	−20,000
Bending moment (kN·m)	−48,232	−96,464	−1,800 (*M*)	−3,600
Torque (kN·m)	40,697	81,394	1,507 (*T*)	3,014
Shear force (kN)	7,086	14,172	800	1,600

Axial and bending forces were applied together by a self-balanced loading system. The eccentric axial loads were applied by four calibrated hydraulic jacks located at the specimen south end by tensioning the 30 high-strength steel bolts along the specimen length direction, as presented in Fig. 3(a). The capacity of hydraulic jacks used in eccentric axial loads application was 2000 kN. Four steel bolts were tensioned each time, and then the jacks were moved to the other four bolts for the next loading application. The torque was applied via tensioning the two vertical high-strength steel bolts through the two calibrated hydraulic jacks with a capacity of 2000 kN that were located at the steel transom east end and concrete transom west end, respectively, as provided in Figs. 3(b and e).

Instrumentation and Measurements Arrangement

As presented in Fig. 3(a), three typical sections of the specimen (B-B, J-J, and C-C) were selected to measure both displacements and strains. Linear variable displacement transducers (LVDTs) were mounted at the bottom of the selected sections. Strain sensors were bonded at the steel–concrete interface to capture the relative slip between the steel plate and UHPC grout. Rosette strain gauges were also mounted on the specimen top and bottom steel plates to record strains in different directions. Fig. 6(a) gives the locations and designation codes for LVDTs and strain gauges at Section J-J. Five representative steel cells located at both the top and bottom slabs were investigated [Fig. 6(a)]. As presented in Fig. 6(b), strain gauges were also mounted on the perforated webs and rebars, while vibrating-wire sensors were embedded in UHPC to monitor the structural behavior of the components inside the cells. All the data was automatically recorded before and after the torque load was applied in each step.

Experimental Results

In this section, vertical displacement at the specimen's bottom slabs, relative slip between the steel plate and UHPC grout, the stress of the specimen's surface plates, load-stress relationships for the UHPC grout, perforated webs, and rebars are summarized and discussed. The stresses described herein are calculated by multiplying the measured strains by the material's modulus of elasticity, where the signs of the compressive stresses are negative and tensile stresses are positive.

Vertical Displacement and Relative Slips

Fig. 7(a) presents the bottom slab vertical displacement of the test specimen. Due to the inherent large torsional stiffness of the PC box girder, the bottom plates rotated clockwise along the east-to-west direction that is consistent with the direction of applied torque through the concrete transom. Experimental results indicated that specimen vertical displacement was small, with a maximum displacement of 8.4 mm occurred at the bottom slab of the PC girder.

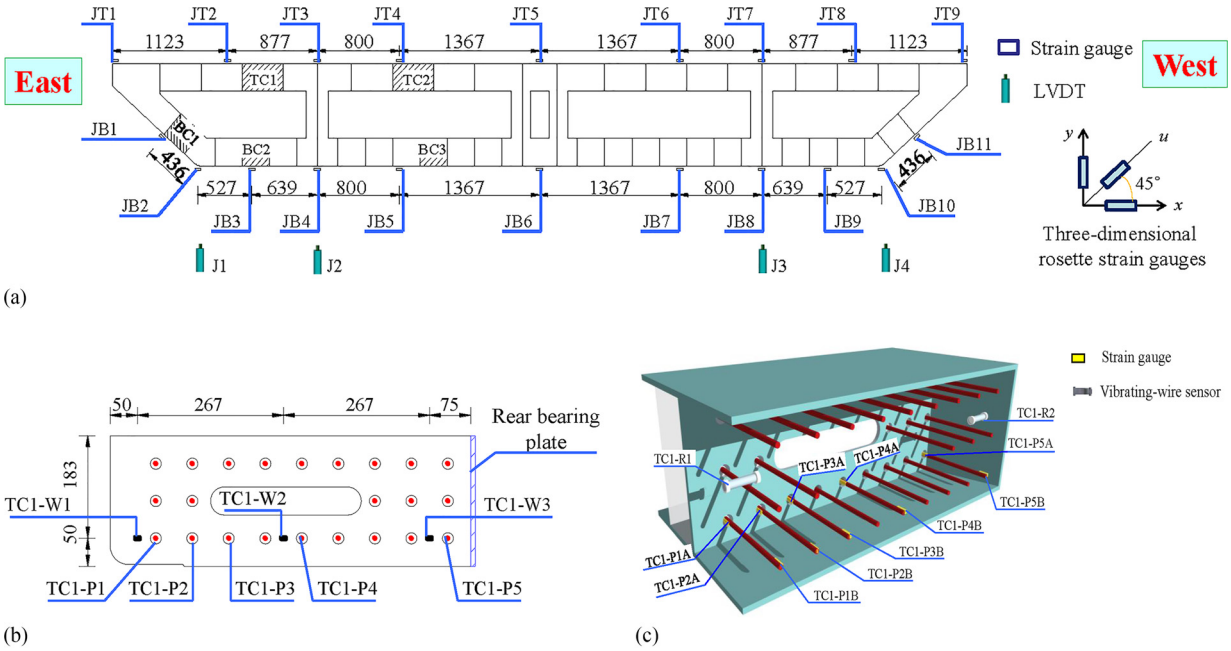

Fig. 6. Measurement positions and codes: (a) strain gauges at surface plates (Section J-J for example); (b) strain gauges at perforated webs; and (c) strain monitor sensors in steel cell. (unit: mm).

The linear displacement distribution along bottom plates indicates the favorable flexural and torsion stiffness of the box cross sections.

Fig. 7(b) presents load-relative slip at the steel plate/UHPC interface. Owing to the negative bending moment, the slip at the bottom steel cells was relatively large as compared to those recorded at the top cells. Under a maximum load of 2.0NMT, the maximum slip obtained from the top and bottom cells were $-12.0\ \mu$m and $-28.0\ \mu$m, respectively. It was noted that the slip gradually increased with the increment of loads and showed a constantly increasing rate, which illustrated the axial stiffness and bearing capacity of the steel–concrete joint with UHPC grout was favorable.

Stresses in Surface Plates of Test Specimen

Stress Distribution on Specimen Surface Plates

Fig. 8 gives the axial stress distribution on surface plates of the selected typical sections. Due to the presence of the negative bending moment, high axial stresses were realized at bottom slabs as compared to those of top slabs. Under the peak load of 2.0NMT, the maximum axial stresses at the PC girder, at the steel–concrete joint, and at the steel girder were −14.7, −57.0, and −133.0 MPa, respectively. The maximum axial stress for the specimen was obtained from the U-shaped stiffeners, with a stress value of −311.0 MPa, which was still under the yield strength of steel stiffeners.

On the other hand, the principal strains in surface plates are computed through the experimental results obtained from rosette strain gauges. The maximum principal stresses in surface plates of the PC girder, steel–concrete joint, and steel girder were −15.1, −68.0, and −142.0 MPa, respectively. Apparently, the stresses in surface plates of the testing specimen under 2.0NMT are smaller than the materials' allowable stress, indicating the favorable bearing capacity of the box cross sections.

Constitutive Analysis of Axial Stress in Specimen Surface Plates

It was noticed that the stresses at the specimen surface steel plates were distributed nonuniformly along the box-section transversal direction. For example, as presented in Fig. 8(a), the axial stresses at the PC girder top slab gradually increased along the transversal direction from east to west, while the axial stresses at the bottom slab showed a continuous decrease along the east-to-west direction. Generally, the axial stress in box-sectional surface plates of the test specimen consists of two parts: (1) the axial stress resulted from axial loads, and (2) the warping stress introduced by the torque. The axial loads produce bilateral symmetrical axial stresses in a bilateral symmetry box cross section; however, the warping stress caused by the application of torque would be antisymmetrical. Consequently, axial stresses at the cross section lateral ends can be evaluated by

$$\sigma^{\kappa} = \sigma_{NM} + \sigma^{k}_{w,\,T} \tag{1}$$

$$\sigma^{\kappa}_{\text{sym.}} = \sigma_{NM} - \sigma^{k}_{w,\,T} \tag{2}$$

where σ^{κ} = axial nominal stress at point k; $\sigma^{\kappa}_{\text{sym.}}$ = axial nominal stress at the symmetric point of k; σ_{NM} = axial stress produced by axial loads; and $\sigma^{k}_{w,\,T}$ = warping stress at point k resulted from torque.

Using Eqs. (1) and (2), the constitutive components of the maximum axial stresses at the selected cross sections under 2.0NMT are analyzed. Fig. 9 presents the values of $\sigma^{k}_{w,\,T}/\sigma^{\kappa}$ at maximum axial nominal stress points. The ratios for the PC and steel girders are comparatively close, with a value ranging from 0.11 to 0.16. For the steel–concrete joint, the $\sigma^{k}_{w,\,T}/\sigma^{\kappa}$ ratios are comparatively high, with a value ranging from 0.19 to 0.27. This may be ascribed to the fact that the σ_{NM} in the joint's surface steel plates was very small due to the occurrence of slip at the steel–UHPC interface, despite the warping constant for the steel–concrete joint was comparatively large and the warping stress $\sigma^{k}_{w,\,T}$ was also small. Accordingly, it could be concluded that axial stress in the specimen's surface plates was mostly governed by the axial and bending forces, and the influence of torque on surface plates axial stress was insignificant.

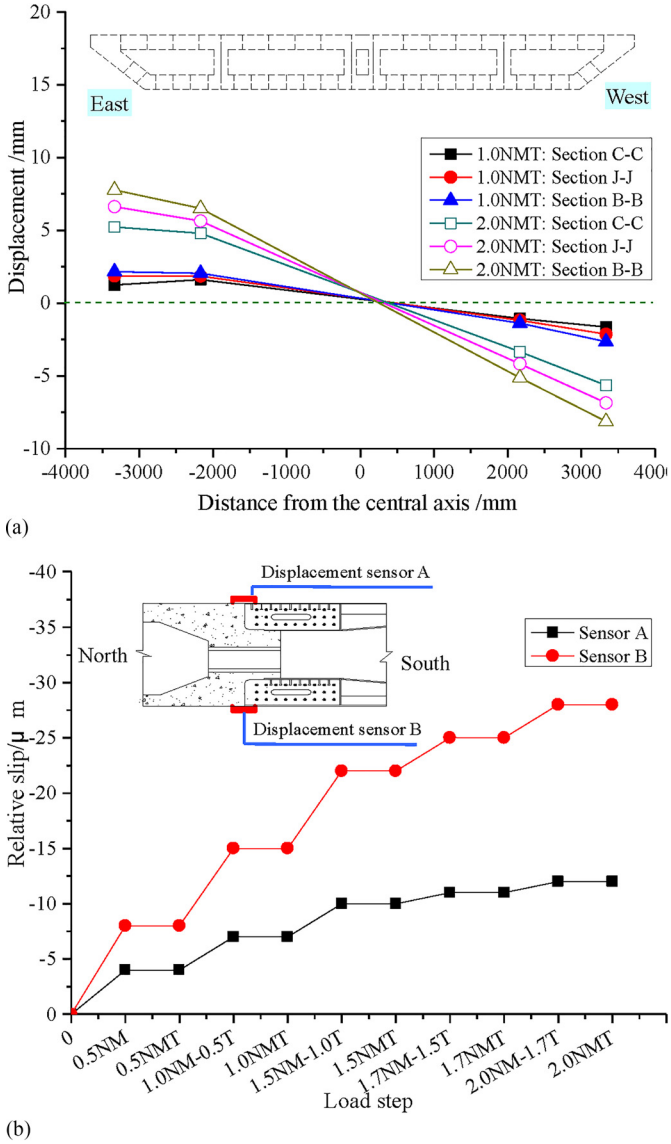

Fig. 7. (a) Vertical displacement on bottom slabs; and (b) relative slip between steel plates and UHPC.

Stresses in the Components of Steel–Concrete Joint

Load-Stress Curves of Surface Plates

Load-stress curves for the surface plates of the steel–concrete joint are presented in Fig. 10. Since the plateau of the majority of the surface steel plates load-stress curves are similar, only the load-stress curves for points at the specimen east end (e.g., JT1 and JB2), west end (e.g., JT9 and JB10), and the middle between the east and west ends (e.g., JT5 and JB6) are displayed in Fig. 10. As shown in this figure, both top and bottom plates showed gradual stress increase with axial and bending loads. As the torque increased, the stresses at both the top plate east end (JT1) and the bottom plate west end (JB10) continually decreased, whereas stress in the bottom plate east end (JB2) and top plate west end (JT9) gradually increased. The load-stress curves of surface plates may explain the stress distribution at the surface plates of the steel–concrete joint [refer to Fig. 8(b)]. The small stress and the almost linear relationship between load and stress reveal the fact that the surface plates behaved within their elastic range, indicating the favorable strength of surface plates in the steel–concrete joint.

Stress of Ultrahigh Performance Concrete Grout

Since experimental results obtained from both the top and bottom cells were similar, only results obtained from UHPC grout at the top cell, TC1, and bottom cell, BC2, [Fig. 6(a)] are presented in Fig. 11. As provided in Fig. 11(a), the measured stresses were all in the form of compressive stresses that gradually increased with the increase of both the axial and bending loads. The stress of the UHPC grout at the bottom steel cell was comparatively higher than those recorded at the top cell due to the presence of the negative moment. Test results showed the minor influence of torque on UHPC stresses. Owing to the large compression area of the UHPC grout, the maximum measured stress of UHPC under a loading protocol 2.0NMT was −5.8 MPa, which is far below the compressive strength of UHPC, indicating that the structural behavior of UHPC grout in the steel–concrete joint is reliable.

Fig. 11(b) presents the UHPC stress distribution. As shown in the figure, the UHPC stress adjacent to the rear bearing plate is small, and maximum stress occurred near the steel–concrete joint and PC girder interface. The continual stress increase from the bearing plate to PC girder can be attributed to the fact that the UHPC adjacent to the steel girder can only carry loads from the bearing plate, while the UHPC, near the PC girder, can resist loads from both the bearing plate and shear connectors. By integrating the compressive stresses of UHPC near the bearing plate with the gross cross-sectional area of the UHPC, the load-transferring ratios for the compression effects between the bearing plate and UHPC grout and the shear connectors were obtained, and the results show that approximately 65 and 35% of the overall loads in steel–concrete joint were transferred by the compression effects of the bearing plate and shearing effects of connectors, respectively.

Stress of Perforated Webs

A summary of the perforated web stresses obtained from TC1 and BC2 [refer to Fig. 7(b)] are presented in Fig. 12. No tensile stresses were measured from the perforated webs during the test, and a negligible stress increment was realized with the application of torque in each step, which implies that the stresses in perforated webs were barely influenced by the torque application. On the other hand, the compressive stress of perforated webs gradually grew with the increase of both the axial and bending loads, reaching a maximum stress of −39.0 MPa under the application of the 2.0NMT loading protocol. Apparently, the stress in perforated webs is far below the yield strength of the steel plate, indicating that the perforated webs introduced to the steel–concrete joint had adequate strength.

The stress distributions of the perforated web along the longitudinal direction are presented in Fig. 12(b). Due to the dispersing efforts of the shear connectors, the perforated web stress near the bearing plate is relatively high as compared to those recorded adjacent to the PC girder, with continual stress degradation along the direction from the bearing plate to PC girder. This observation also is in agreement with experimental observations reported by He et al. (2014), Zhang et al. (2010b), and Liu et al. (2010) for perforated webs in steel–concrete joints fabricated with conventional concrete. The comparatively high stress of the perforated webs near the bearing plate further demonstrates that connectors in the steel–concrete joint effectively disperse loads between different materials.

Stress of Perforated Rebars

As can be seen in Fig. 6(c), each perforated rebar is mounted with two strain gauges: one by the hole center (e.g., TC1-P1A), and the other by the middle of two adjacent perforated webs (e.g., TC1-P1B). Fig. 13(a) shows load-stress curves of perforated rebars in the TC1 and BC2. The tensile stress in perforated rebars gradually

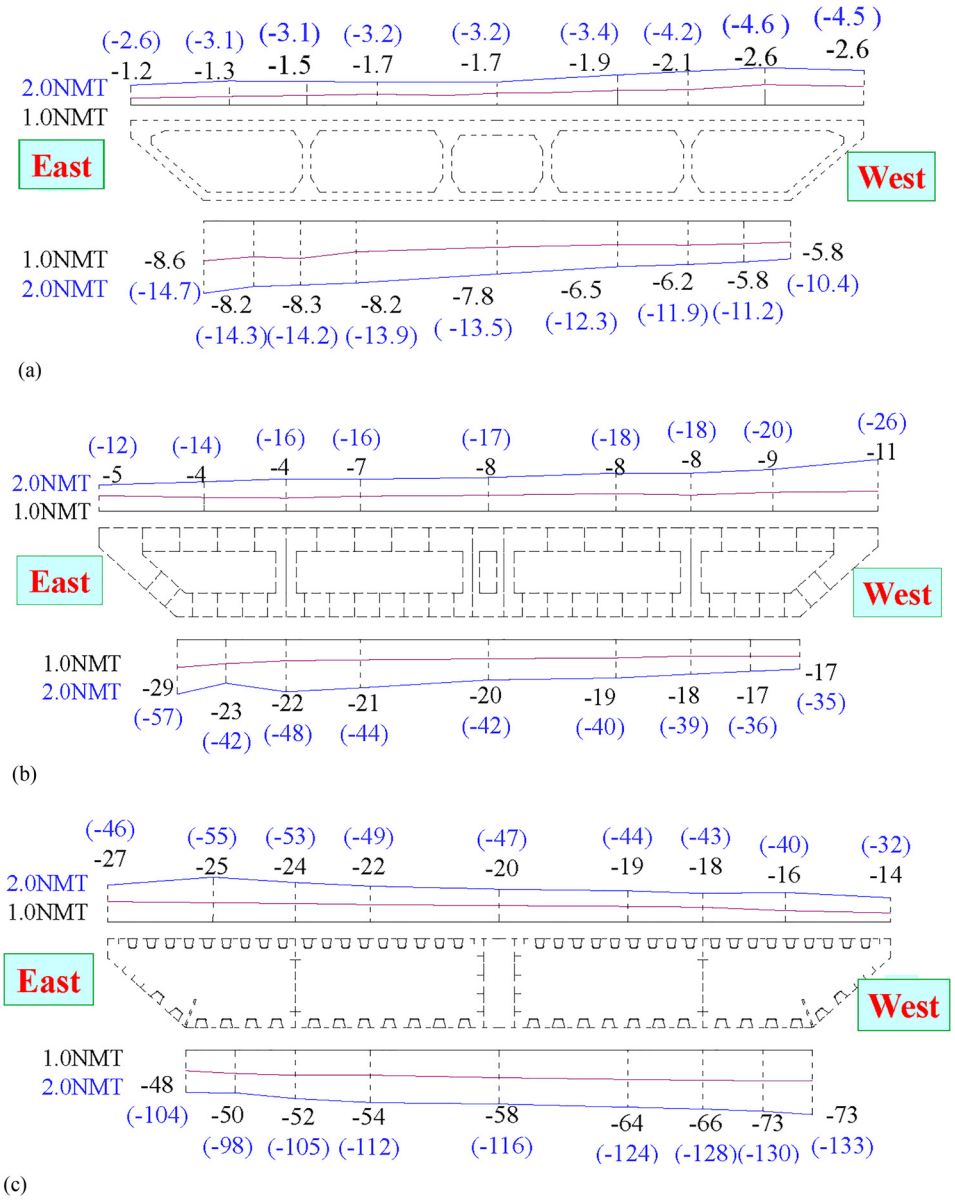

Fig. 8. Axial nominal stress distributions: (a) PC girder (C-C); (b) steel–concrete joint (J-J); and (c) steel girder (B-B).

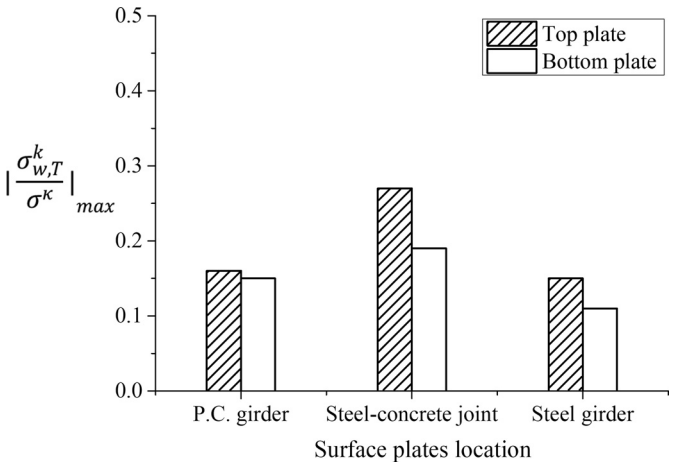

Fig. 9. Constitutive analysis of axial stress in surface plates.

increased with the growth of axial and bending loads, and the impact of the torque on perforated rebars was insignificant. The maximum stress of perforated rebars under 2.0NMT was 62.0 MPa, which was about one-fifth of the yield strength of HRB335 steel rebar. It was noted that the stress obtained from strain gauges at the hole center was much larger than those in the middle of adjacent webs. This is understandable because the force from perforated webs transferred to the UHPC grout via a combined tension/bending action of the rebars directly at the hole center, whereas the rebars inside steel cells were mainly used to anchor the rebars at the hole (He et al. 2016, 2017). The comparatively small stress indicates that the perforated rebar, which contributes to the shear capacity of a PBL connector, is played out to two times the design load of the steel–concrete joint without incurring any yielding to the reinforcements itself.

The stress distribution along the longitudinal direction is given in Fig. 13(b). The perforated rebar stress near the bearing plate continually increased along the direction from the bearing plate to the PC

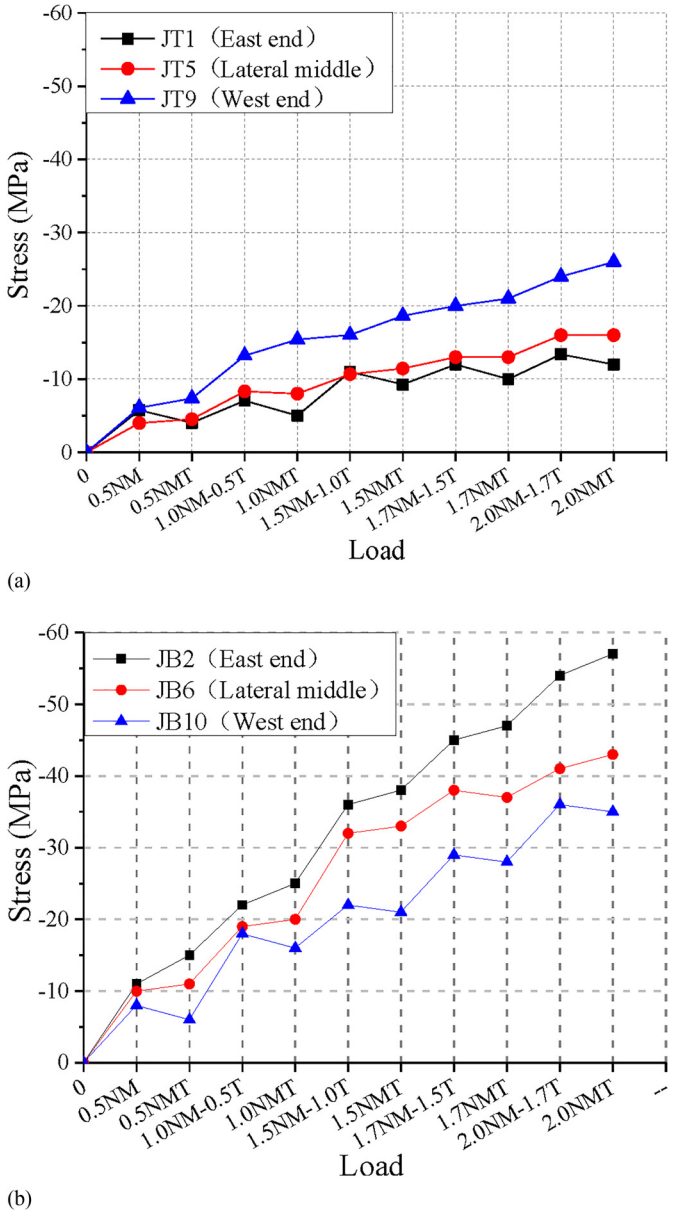

Fig. 10. Load-stress curves for surface plates of steel–concrete joint at (a) top steel plate; and (b) bottom steel plate.

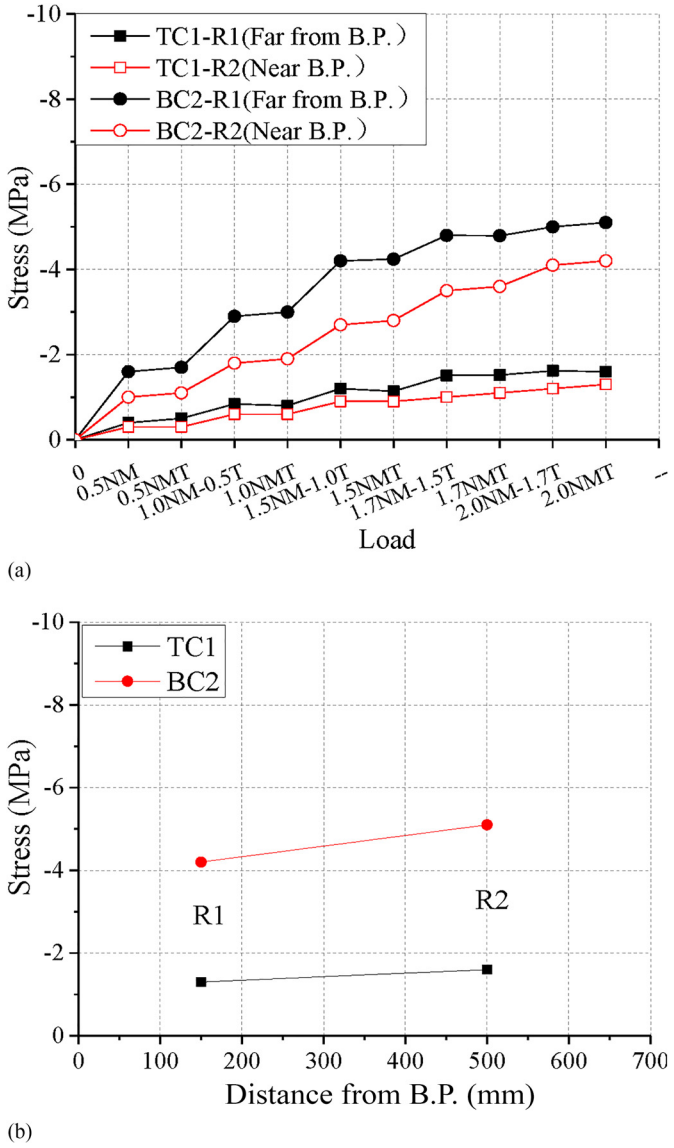

Fig. 11. Stress of UHPC grout in steel cells: (a) load-stress relationship for UHPC in steel cells (TC1 and BC2); and (b) stress distribution for UHPC in steel cells (TC1 and BC2).

girder. The comparatively high stress near the PC girder reveals that more loads dispersed from steel to UHPC grout via the PBL far away from the steel bearing plate. This may be because the deformation of the PBL adjacent to the bearing plate is seriously restrained by the bearing plate, and the PBL far away from the bearing plate could produce a comparatively large deformation due to the compressive deformation of the UHPC grout.

Finite-Element Analysis

Numerical Simulation of Steel–Concrete Joint

General

A numerical study based on finite-element (FE) code ANSYS 17.1 was conducted to simulate the behavior of the steel–concrete joint with UHPC grout under the combined actions. As presented in Fig. 14, three-dimensional eight-node solid elements (Solid95) were used for modeling the PC girder and UHPC grout. The steel girder, steel plates of steel–concrete joint, and the transoms were modeled by the four-node shell elements (Shell181). The most critical zone in which force transferred between different materials is the steel–concrete joint zone, where a finer mesh with a nominal element size of approximately 40.0 mm was used, as compared to a coarser mesh, with the nominal element size of approximately 80.0 mm.

In the numerical model, the bottom surface, which contacted the ground, of the steel transom was restrained against all translational degrees of freedom. On the other hand, the bottom surface of the concrete transom was restrained against all the translational degrees of freedom except for the longitudinal translational degree of freedom. At the contact surface of the steel girder and steel–concrete joint, nodes associated with UHPC and the rear bearing plate were coupled together. By doing so, the bearing plate elements could have all translational degrees of freedom equal to those of the UHPC element near them. Force-controlled loading was applied on the surface of the transoms.

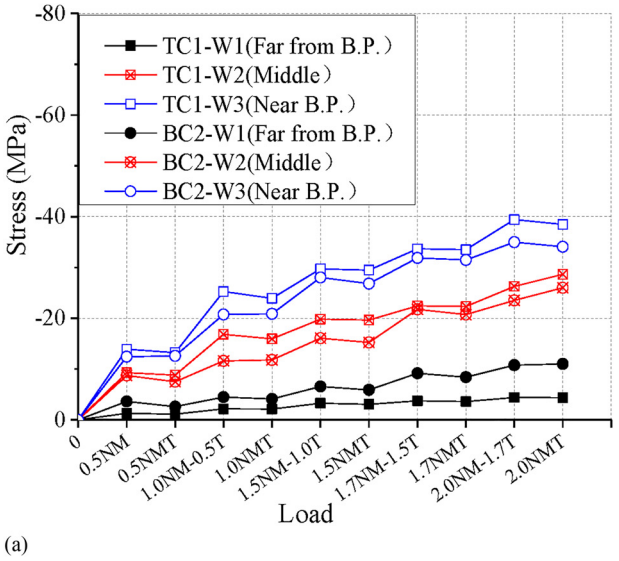

Fig. 12. Stress of perforated webs: (a) load-stress curves of perforated webs (TC1 and BC2); and (b) stress distribution on perforated webs (TC1 and BC2).

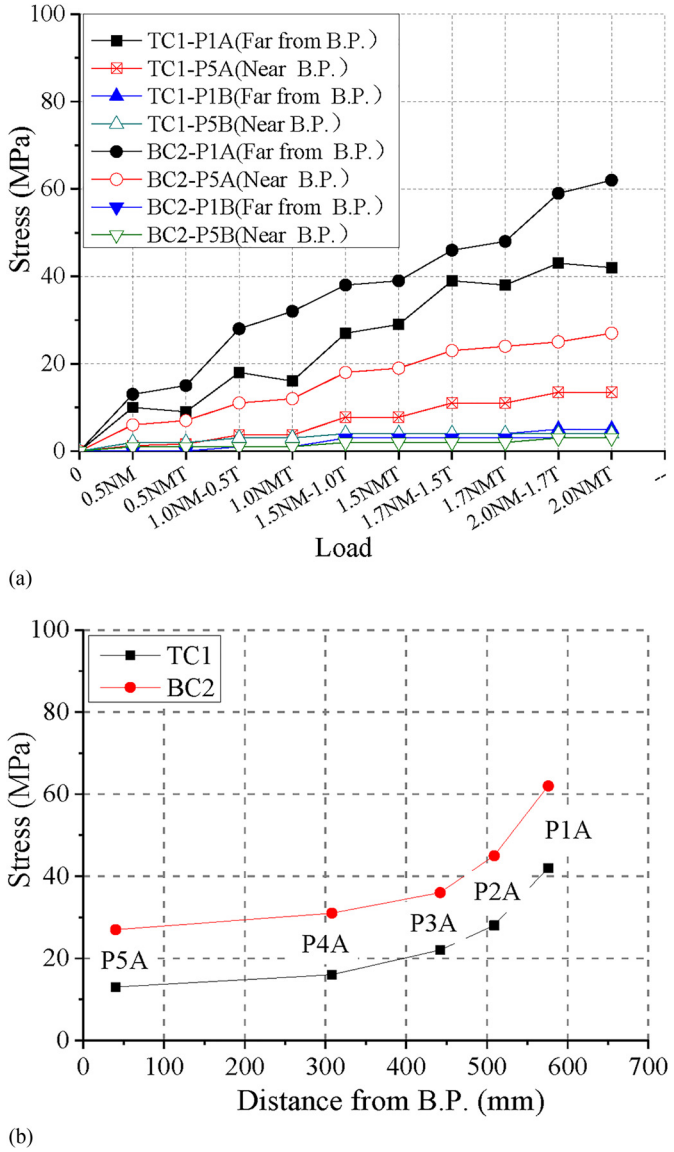

Fig. 13. Stress of perforated rebars: (a) load-stress relationship for perforated rebars (TC1 and BC2); and (b) stress distribution on perforated rebars (TC1 and BC2).

Friction at the interface of UHPC/top and bottom steel plates of steel cells was formulated by contact discretization (Elements Conta174 and Targe170) provided in ANSYS 17.1. In a contact pair, the surface associated with UHPC grout was taken as the target surface, and the other surface of the contact associated with the steel plates was taken as the subordinate surface. In this analysis, a friction coefficient of 0.5 was taken for the contacting surfaces (Zheng et al. 2016).

Shear Connector Modeling

In order to simplify the simulation, two-node nonlinear spring elements (Combin39) were utilized for the simulation of shear connectors, including the PBL and the steel studs. The mechanical property for steel studs is determined by the following equations, which were reported by Cheng et al. (2016):

$$\frac{P}{P_u} = \frac{S}{S+c} \tag{3}$$

$$P_u = \min\left(0.47A_s\sqrt{E_c f_c},\ A_s f_u/\eta\right) \tag{4}$$

where P = force at any point (N); S = slip corresponding to P (mm); P_u = shear capacity of a stud (N); c = coefficient determined by the initial stiffness, $c = P_u/4.08 \times 10^{-5} d^2 E_c$; A_s = cross-sectional area of stud (mm^2); E_c = Young's modulus of concrete (MPa); f_c = concrete compressive strength (MPa); f_u = ultimate strength of stud (MPa); η = coefficient associated with diameter, $\eta = 2 - 1.2 \times 10^{-4} E_c/d^{0.5}$; and d = diameter of stud shank (mm).

The force-deformation curves for PBL are defined by the formulas developed by Cheng et al. (2016).

$$\frac{P}{P_u} = \frac{S}{S+c} \tag{5}$$

$$c = \frac{P_u}{2 \times 4.08 \times 10^{-5} d_s^2 E_c + 5 \times 10^{-7} t\left(d_h^2 - d_s^2\right) E_c} \tag{6}$$

where d_h = diameter of the rib holes (mm); t = thickness of perforated ribs (mm); d_s = diameter of transverse rebar (mm); and E_c = elastic modulus of concrete (MPa).

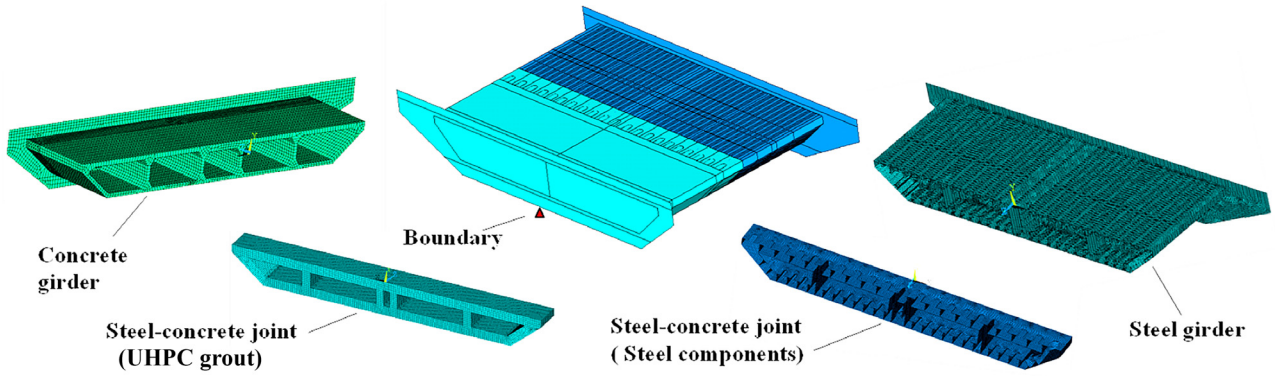

Fig. 14. Finite-element models of steel–concrete joint.

The shear bearing capacity, P_u, for a PBL embedded in UHPC grout is specified in a previous work by He et al. (2017).

$$P_u = \tau_b A_b + \left(1.06 + 0.07 V_f \frac{L_f}{\phi_f}\right) \frac{\pi(D^2 - d^2)}{4} f_{cu} + 2.09 A_s f_y \tag{7}$$

where τ_b = residual bond stress between the perforated steel plate and normal concrete, $\tau_b = \left(0.04 + 0.04 V_f L_f / \phi_f\right)\sqrt{f_{cu}}$ (MPa); A_b = area of the contact surface between the steel plate and the concrete (mm^2); V_f = volume content of fibers; L_f = average length of fibers (mm); ϕ_f = normalized diameter of fibers (mm); D = diameter of the hole (mm^2); d_s = diameter of the transverse rebar through the hole (mm); and f_{cu} = concrete cubic compressive strength (MPa).

Material Modeling

Concrete. Stress-strain relationships for concrete in compression and in tension were adopted to depict concrete properties. The relation between stress (σ_c) and strain (ε_c) for concrete materials in compression suggested by the Chinese code (China Committee for Standardization 2011) is described by the following equations:

$$\text{For } \varepsilon_c \le \varepsilon_0: \qquad \sigma_c = \left[1 - (1 - \varepsilon_c/\varepsilon_0)^n\right] f_c \tag{8}$$

$$\text{For } \varepsilon_0 < \varepsilon_c \le \varepsilon_{cu}: \qquad \sigma_c = f_c \tag{9}$$

$$n = 2 - \frac{1}{60}(f_{cu,k} - 50) \tag{10}$$

$$\varepsilon_0 = 0.002 + 0.5(f_{cu,k} - 50) \times 10^{-5} \tag{11}$$

$$\varepsilon_{cu} = 0.0033 - (f_{cu,k} - 50) \times 10^{-5} \tag{12}$$

where ε_c = strain at any stress σ_c; ε_0 = peak strain defined as the strain corresponding to the concrete compressive strength f_c; $\varepsilon_0 = 0.002$ when the computed $\varepsilon_0 < 0.002$; f_c = prism compressive strength of concrete; $f_{cu,k}$ = cubic compressive stresngh of concrete; ε_u = ultimate compressive strain, $\varepsilon_u = 0.0033$ when the computed ε_u larger than 0.0033; and n = coefficient, not larger than 2.

The tensile strength of concrete suggested by FIB MC 2010 (FIB 2012) was determined by Eq. (13).

$$f_t = 0.3 f_c^{2/3} \tag{13}$$

A linear σ_t-ε_t curve was used for all concrete materials in tension. After the strain exceeds the crack strain ε_{cr} corresponding to peak stress, the stress of normal concrete linearly decreases to zero at total strain of ten times the strain at tensile cracking (Wang 2011). For the RPC material with short steel fibers, the stress at the post-cracking stage remains constantly at the value of peak stress until the strain reaches up to 0.001 (Hunan Province Dept. of Housing and Urban-Rural 2017).

Steel. The compression and tension stress-strain curve for steel plates were consistent. A linear elastic and fully plastic bilinear σ_t-ε_t material model was adopted for steel plates. The yield strength and elastic modulus of steel were taken as the results obtained in the aforementioned model tests (refer to Table 3).

Validation of Numerical Model

Numerical stress results at the surface plates under the 2.0NMT loading protocol are given in Fig. 15, along with the experimental results. As shown in Fig. 15(a), the predicted stresses at the PC and steel girders surface plates correlated well with the experimental results, with an average deviation between the experimental and numerical stresses of 11%. Fig. 15(b) presents the surface plates of the steel–concrete joint stress distribution. The corresponding deviation for surface plates of the steel–concrete joint was comparatively large as compared to those measured at the PC and steel girders, showing an average ratio of 14%. The main reason for this large value may be attributed to the steel plate–UHPC interface contact differences in the experiments and in the numerical models. Overall, the favorable correlations between experimental and numerical results demonstrated that the established model is reliable for predicting the structural behavior of the surface plates of the model.

A comparison between the numerical and experimental axial stresses results of the steel–concrete joint elements are summarized in Fig. 16. As presented in Fig. 16(a), under the peak load of 2.0NMT, stresses in the perforated webs were relatively large near the bearing plate, and the stress distribution curve obtained from numerical models was verified by the experimental points. Fig. 16(b) indicates that UHPC simulated stresses near the bearing plate are comparatively small as compared to those obtained from the UHPC near the PC girder.

Now, by integrating the axial stress of UHPC grout and steel cells near the bearing plate, it was found that approximately 63 and 37% of the overall axial forces were carried by the UHPC grout and steel members, respectively. These results are also considerably correlated with the experimental results. Although the difference between the numerical stress-strain curve and experimental points were observed, the numerical results still showed considerable accuracy to reflect the load transfer feature of the UHPC grout in the steel–concrete joint.

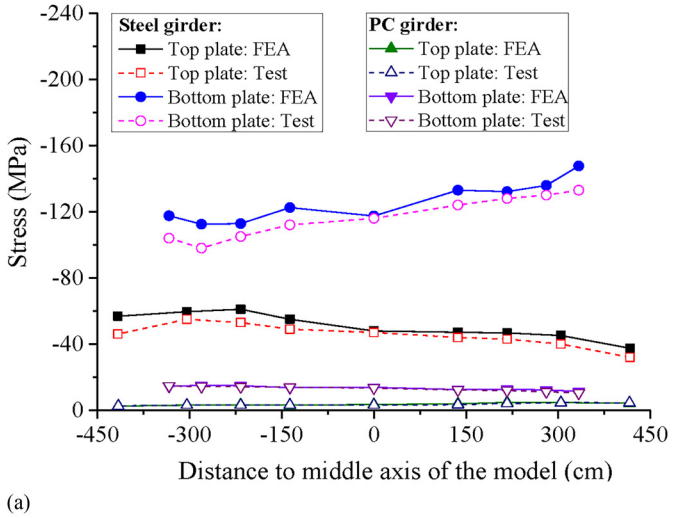

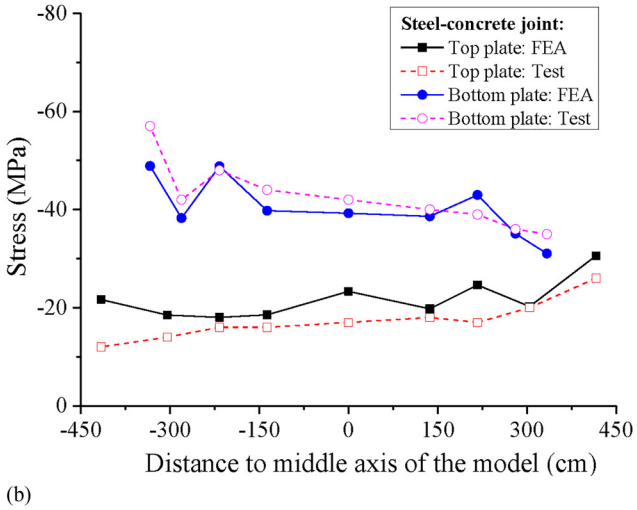

Fig. 15. Distribution of stress on surfaces plates—experimental versus numerical: (a) PC and steel girders; and (b) steel–concrete joint.

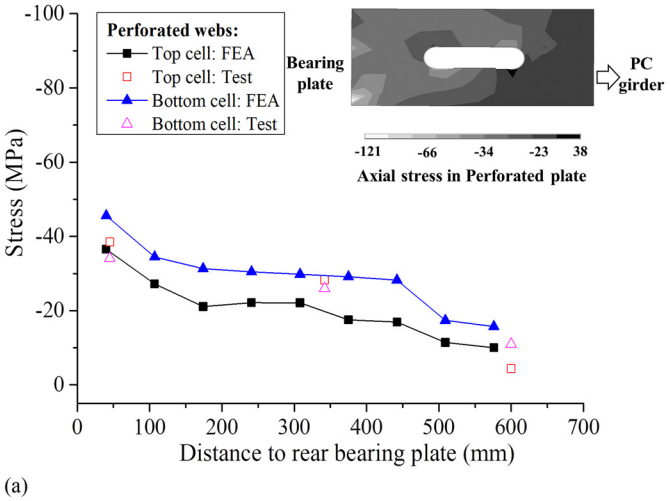

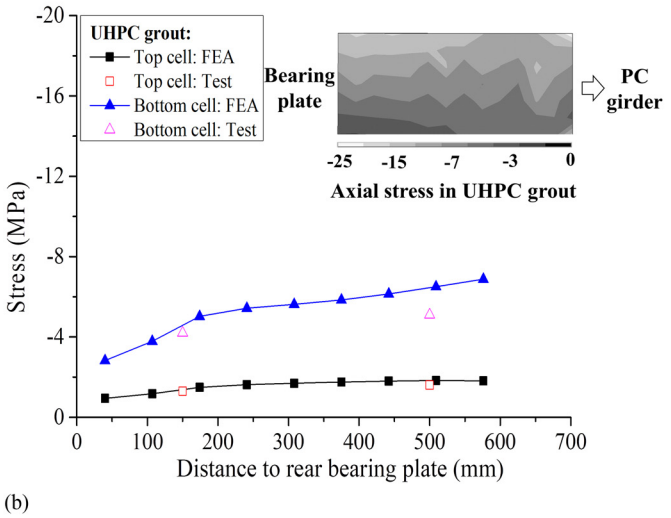

Fig. 16. Stress of steel–concrete joint from experimental and numerical results: (a) stress of perforated webs; and (b) stress of UHPC core grout.

Parametric Analysis

Analytical Model

The preceding comparisons confirmed the validity of the numerical model in simulating the experimental test results; however, the longitudinal prestressing forces were not considered in the numerical model because the experimental strains did not include the strain produced by the prestressing forces. In order to evaluate the load transfer mechanism of the steel–concrete joint under actual loads, along with the two times design load, longitudinal prestressing forces used in the actual bridge, considering the scale ratio, were adopted in the numerical model. Table 5 presents a summary of the applied loads. A total of six models with steel cell heights of 140.0, 160.0, 180.0, 200.0, 230.0, and 250.0 mm were established. The minimum height value of 140.0 mm was adopted because a smaller steel cell height would lead to serious fabrication difficulties for the steel–concrete joint construction of an actual bridge.

Simulation Results

As determined by both the experimental and numerical results, due to the despering effects of PBL connector groups, the stresses of the UHPC grout near the PC girder gradually decreased to that adjacent to the bearing plate, and that of perforated webs near the PC girder showed a gradual increase along this direction. In addition, owing to the hogging moment, steel–concrete joint stresses at the bottom steel cells are comparatively higher than those generated at the top cells. The average stress of UHPC grout near the PC girder and that of perforated webs near the bearing plate in a bottom cell (BC2) are extracted and summarized in Fig. 17. As shown in the figure, the stress of UHPC grout gradually dropped with the steel cell height. As the cell height increased from 140.0 to 250.0 mm, the average stress of UHPC grout and perforated plates decreased by 37 and 46%, respectively. It should be noted that the stress decreasing rate of UHPC grout kept constantly with the growth of height. On the other hand, the changes in decreasing

Table 5. Applied forces for the parametric analytical model

Name	Axial force (kN)	Bending moment (kN·m)	Torque (kN)
2.0NMT	−20,000	−3,600	3,014
Prestressing loads	−19,080	−2,180	—

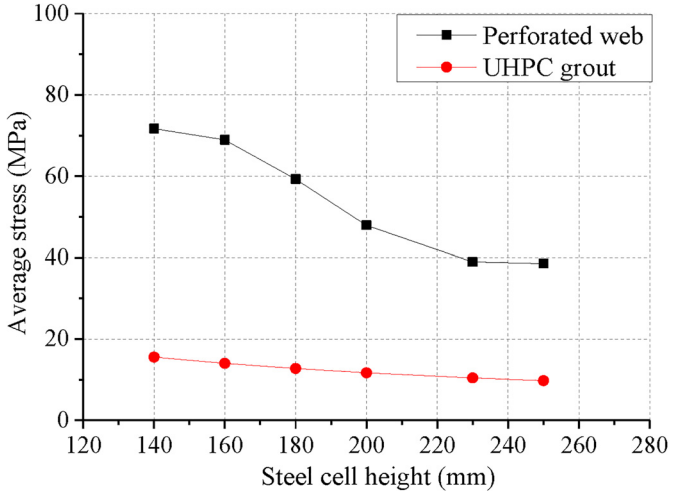

Fig. 17. Comparison of average stresses in the joint components with varying steel cell heights.

rate of perforated webs are found to be comprehensive. As the steel cell height increased from 140.0 to 160.0 mm, the stresses generated at the perforated webs decreased by 3.8%; after the height exceeded 160.0 mm and continually increased up to 230.0 mm, the stress decreasing ratio rapidly increased with an average decreasing ratio of approximately 17%. This may be ascribed to the fact that more internal forces transferred to UHPC grout by the bearing steel plate with the steel cell cross-sectional area gradually increased. The maximum stress obtained from a model with cell height of 140 mm is −41.2 MPa for UHPC grout and −140.8 MPa for perforated webs, which are below the design strength of the UHPC grout and the steel plate. Obviously, the high strength of UHPC grout enables the possibility of using steel cells with small height in the steel–concrete joint of hybrid cable-stayed bridges.

Fig. 18 gives the average shear force transferred by a PBL and a steel stud connector with different cell heights. As can be seen, due to the weakened steel cell restraints, the average shear force of the PBL and steel stud continually decrease with the increment of steel cell height. With the steel cell height increased from 140.0 to 250.0 mm, the shear force of the PBL and steel stud decreased by 18 and 27%, respectively. Fig. 18(b) gives the ratio between the maximum shear force of a connector and its predicting resistance. The maximum shear force of a connector was extracted from the parametric analytical models, while the theoretical shear resistance of steel studs and PBL are computed by Eqs. (4) and (7), respectively. It shows that all ratios for PBL and steel studs are under 0.5, indicating the connectors embedded in UHPC grout did not utilize their ultimate strength. With steel cell heights ranging from 140.0 to 250.0 mm, the maximum ratios for PBL and steel studs are 0.25 and 0.47, respectively. The relative small ratios reveal the fact that owing to the lacking of practical design methods for steel–concrete joints, redundant numbers of connectors have been adopted in existing hybrid girder bridges.

Table 6 summarizes the load-carrying ratio by bearing plate compression effects and shear connectors with various cell heights. In the table, all models classified by the steel cell height show a similar trend, namely, that the load ratio by the bearing plate slightly increases with the height. Due to the longitudinal prestressing strands directly anchored on the bearing plate [refer to Fig. 3(a)], the bearing plate played a major role in axial load transfer, with a ratio of approximately 80%. The load ratio for the bearing plate

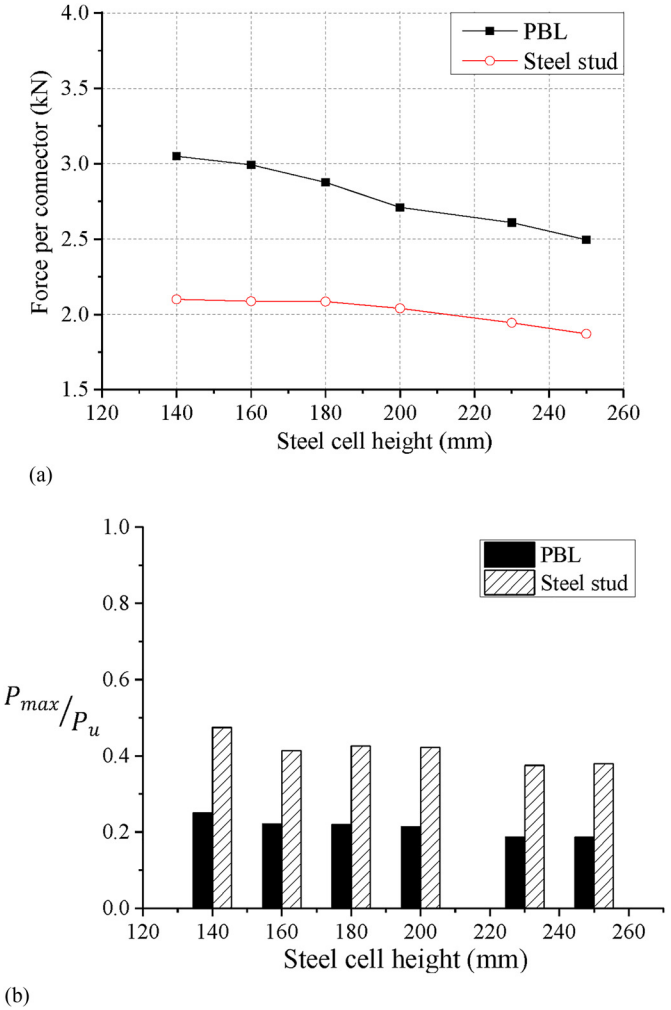

Fig. 18. Forces in shear connectors with varying steel cell heights: (a) average forces of connectors versus steel cell heights; and (b) efficiency ratio of connectors.

Table 6. Load ratio of bearing plate and shear connectors with varying steel cell height

	Steel cell height (mm)					
Load ratio (%)	140	160	180	200	230	250
Bearing plate in compression	79.5	80.7	80.9	81.4	82.5	82.9
Connectors in shear	20.5	19.3	19.1	18.6	17.5	17.1
Sum	100.0	100.0	100.0	100.0	100.0	100.0

increased by 3.4% when the cell height increased from 140.0 to 250.0 mm. Generally, reducing the height of steel cells suitably leads to a better utilization of shear connectors, makes the transition of stiffness between the steel girder and PC girder smoother, and results in a more economical joint structure.

Assessment of the Steel–Concrete Joint with Ultrahigh Performance Concrete Grout

The proposed steel–concrete joint detail with UHPC grout presented both excellent workability and structural behavior. The UHPC grout without coarse aggregates was easily poured into the

cells. No visible separation between the steel plate and UHPC grout was observed during the test. Under the experimental peak load of two times the design forces, the maximum stresses in the steel–concrete joint were under the allowable value of stress for the materials. Also, both experimental and numerical results revealed that the PBL connectors in the studied joint did not utilize their shearing capacity under the maximum design loads. Generally, PBL connectors in steel–concrete joints failed in a tension-bending failure mode (Su et al. 2014; Wang et al. 2014; He et al. 2016, 2018). Wang et al. (2014) found that the ultimate tensile strain for transverse reinforcement under the tension-bending failure can reach to1400 $\mu\varepsilon$. The maximum strain measured from reinforcements in the present test was 265 $\mu\varepsilon$, only accounting for 19% of its ultimate tensile strain. In order to properly determine the dimensions and the number of PBLs in steel–concrete joints with UHPC grout, practical methods for determining the axial load dispersed by shear connectors need to be further investigated in future studies.

Conclusions and Recommendations

This paper presents experimental and numerical results of a steel–concrete joint with UHPC grout in single cable–plane hybrid cable-stayed bridges. The applicability of the UHPC grout and the efficiency of the steel–concrete joint with the UHPC are evaluated. Numerical simulation results provided an insight into the load-transferring mechanisms of the steel–concrete joint. The main conclusions from the study are as follows:

1. The UHPC grout used in the steel–concrete joint resulted in reducing the difficulty of pouring concrete into the cells, and the joint with UHPC exhibited favorable combined behavior and adequate strength when subjected to the axial compression, flexure, and twisting moments.
2. Structural behavior of the steel–concrete joint with UHPC grout was mainly governed by the axial and bending forces, and the influence of torque was insignificant. The large compression area and short load transferring path enabled the steel bearing plate to carry 65% of the overall force in the studied joint, while the remaining 35% force was dispersed by shear connectors.
3. Internal force distribution of shear connectors in steel–concrete joint is dependent on the relative slip at the steel cells–UHPC interface. The lacking of practical design methods for steel–concrete joint leads to the redundant adoption of PBLs. The maximum shear force of PBLs obtained from experimental results only accounted for 20% of their ultimate strengths under design loads.
4. Parametric study results indicated that reducing the height of the steel cell suitably leads to a better utilization of shear connectors, a smoother stiffness transition between the steel and PC girders, and a more economical joint structure. The outcomes of this study can be served as a reference for the application of UHPC grout in the steel–concrete joint of hybrid cable-stayed bridges.

This study focused on the behavior of the steel–concrete joint with UHPC grout under static combined axial force, bending moment, and torque-loading protocol. However, due to the site testing facilities limitations, only the elastic behavior of the studied steel–concrete joint was discussed. In addition, the influence of creep, shrinkage, and thermal effects on the performance of such joints are essential. For this reason, further studies on these effects are recommended.

Acknowledgments

This research is sponsored by the National Natural Science Foundation of China (Grant 51278182 and 51408213), and the program of China Scholarship Council (File 201506130024). These financial supports are gratefully acknowledged. The support of the Civil & Environmental Engineering Department at the University of California, Irvine, is also acknowledged.

References

Chandra, V., A. Ricci, P. Towell, and K. Donington. 2003. "Landmark cable-stayed bridge over the Charles River, Boston, Massachusetts." *J. Transport. Res. Rec.* 1845 (1): 19–27. https://doi.org/10.3141/1845-03.

Cheng, X., X. Nie, and J. Fan. 2016. "Structural performance and strength prediction of steel-to-concrete box girder deck transition zone of hybrid steel-concrete cable-stayed bridges." *J. Bridge Eng.* 21 (11): 1–19. https://doi.org/10.1061/(ASCE)BE.1943-5592.0000958.

China Committee for Standardization. 2011. *Code for design of concrete structures*. [In Chinese.] Rep. No. GB 50010-2010. Beijing: China Architecture and Building Press.

China Committee for Standardization. 2014. *Steel strand for prestressed concrete*. [In Chinese.] Rep. No. GB/T 5224-2014. Beijing: Standard Press of China.

Endo, T., T. Lijima, and A. Okuakawa. 1991. "The technical challenge of a long cable-stayed bridge—Tatara Bridge." In *Proc., Seminar on Cable-stayed Bridges: Recent Developments and Their Future*, 417–436. Amsterdam, Netherlands: Elsevier.

Fédération Internationale Du Béton (FIB). 2012. *Model code 2010-Final draft.* Lausanne, Switzerland: FIB Bulletin Nos. 65/66.

Gimsing, N. J. 1997. *Cable supported bridges: Concept and design.* Chichester, UK: Wiley.

He, S., Z. Fang, Y. Fang, M. Liu, L. Liu, and A. Mosallam. 2016. "Experimental study on perfobond strip connector in steel–concrete joints of hybrid bridges." *J. Constr. Steel Res.* 118 (Mar): 169–179. https://doi.org/10.1016/j.jcsr.2015.11.009.

He, S., Z. Fang, and A. Mosallam. 2017. "Push-out tests for perfobond strip connectors with UHPC grout in the joints of steel-concrete hybrid bridge girders." *Eng. Struct.* 135 (Mar): 177–190. https://doi.org/10.1016/j.engstruct.2017.01.008.

He, W., Y. Liu, and R. Wang. 2012. "Analysis of joint section structure of hybrid girder of Jiujiang Changjiang River Highway Bridge." [In Chinese.] *Bridge Constr.* 42 (1): 30–35.

He, J., Y. Liu, and B. Pei. 2014. "Experimental study of the steel-concrete connection in hybrid cable-stayed bridges." *J. Perform. Constr. Fac.* 28 (3): 559–570. https://doi.org/10.1061/(ASCE)CF.1943-5509.0000444.

He, S., A. Mosallam, Z. Fang, C. Zou, W. Feng, and J. Su. 2018. "Experimental study on CFSC encased shear connectors in steel-concrete composite joints with UHPC grout." *Constr. Build. Mater.* 173 (Jun): 638–649. https://doi.org/10.1016/j.conbuildmat.2018.04.086.

Hunan Province Dept. of Housing and Urban-Rural. 2017. Technical specification for reactive powder concrete structures. [In Chinese.] Rep. No. DBJ43/T325-2017. Changsha, China: China Architecture and Building Press.

Ji, J., C. Mi, and X. Cao. 2009. "Design and research on mix proportioning for C55 high performance concrete of hybrid girder cable-stayed bridge." [In Chinese.] *Bridge Constr.* 36 (1): 39.

Leonhard, F., W. Andra, and H. P. Andra. 1987. "New, improved bonding means for composite load bearing structures with high fatigue strength." [In German.] *Beton-und Stahlbetonbau* 82 (12): 325–331. https://doi.org/10.1002/best.198700500.

Liu, R., and Y. Liu. 2015. "Analysis of auxiliary ribs in steel-concrete joint of hybrid girder." *J. Constr. Steel Res.* 112 (Sept): 363–372. https://doi.org/10.1016/j.jcsr.2015.05.015.

Liu, R., J. Yu, and Y. Liu. 2010. "Mechanical analysis of joint sections of hybrid girder of Edong Changjiang River Bridge." [In Chinese.] *Bridge Constr.* 33 (1): 35.

Nie, J. 2011. *Steel-concrete composite bridges*. [In Chinese.] Beijing: China Communications Press.
Ohlsson, S. 1996. "Model testing of the Tjorn Bridge." In *Proc., 4th Int. Model Analysis Conf*., 599–605. Schenectady, New York: Union College.
Qin, W., and F. Cao. 1999. "A new ultra-high performance concrete-reactive powder concrete." [In Chinese.] *Ind. Constr.* 29 (4): 16–18. https://doi.org/10.13204/j.gyjz1999.04.005.
Su, Q., W. Wang, H. W. Luan, and G. Yang. 2014. "Experimental research on bearing mechanism of perfobond rib shear connectors." *J Constr. Steel Res.* 95 (Apr): 22–31. https://doi.org/10.1016/j.jcsr.2013.11.020.
Virlogeux, M. 1994. "The Normandie Bridge, France: A new record for cable-stayed bridges." *Struct. Eng. Int.* 4 (4): 208–213. https://doi.org/10.2749/101686694780601629.
Volke, E. 1973. "The current pressure in the case of the Nordbrucke Mannheim-Ludwigshafen (Kurt-Schumacher bridge)." [In German.] *Teil 1: Konstruktion und Statik, Stahlbau* 42 (4): 97–104.
Wang, X. 2011. *Ansys structural analysis-numerical simulation.* [In Chinese.] Beijing: China Communications Press.
Wang, W., C. Zhao, Q. Li, and W. Zhuang. 2014. "Study on load-slip characteristic curves of perfobond shear connectors in hybrid structures." *J. Adv. Concr. Technol.* 12 (10): 413–424. https://doi.org/10.3151/jact.12.413.
Yao, Y., Q. Pu, and C. Yao. 2014. "Research on the equivalence and the mechanical performance of the model of steel-concrete joint." *Appl. Mech. Mater.* 578–579: 168–172. https://doi.org/10.4028/www.scientific.net/AMM.578-579.168.
Ye, S., M. Zhang, and L. Zhu. 2015. "Analysis of impact of steel-concrete joint section disengagement of railway cable-stayed bridge." [In Chinese.] *Int. Bridge* 43 (4): 58–62.
Zhang, Z., C. Huang, and Z. Dang. 2010a. "Static experiments of steel-concrete composite structure of hybrid cable-stayed bridges." [In Chinese.] *J. Huazhong Univ. Sci. Technol.: Natural Science Ed.* 38 (4): 121–124.
Zhang, Z., C. Huang, and H. Xu. 2010b. "Force transfer mechanism for steel-concrete composite structures of hybrid cable-stayed bridges." [In Chinese.] *J. Huazhong Univ. Sci. Technol.: Natural Science Ed.* 38 (5): 117–120.
Zhang, Y., X. Li, and X. You. 2014. "Construction technology of Jiu-Jiang Yangtze River Highway Bridge." *Appl. Mech. Mater.* 501–504: 1274–1278. https://doi.org/10.4028/www.scientific.net/AMM.501-504.1274.
Zhang, Q., and B. Wu. 2013. "Model test study of steel and concrete joint section of Jiujiang Changjiang River Highway Bridge." [In Chinese.] *Bridge Constr.* 43 (5): 68–74.
Zheng, S., Y. Liu, and T. Yoda. 2016. "Parametric study on shear capacity of circular-hole and long-hole perfobond shear connector." *J. Constr. Steel Res.* 117 (Feb): 64–80. https://doi.org/10.1016/j.jcsr.2015.09.012.